














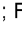





RESEARCH ARTICLE | OCTOBER 12 2023

Characterizing the multi-dimensional reaction dynamics of dihalomethanes using XUV-induced Coulomb explosion imaging

T. Walmsley ; J. Unwin ; F. Allum ; S. Bari ; R. Boll ; K. Borne; M. Brouard ; P. Bucksbaum; N. Ekanayake ; B. Erk ; R. Forbes ; A. J. Howard; P. Eng-Johnsson ; J. W. L. Lee; Z. Liu; B. Manschwetus ; R. Mason; C. Passow ; J. Peschel; D. Rivas; D. Rolles ; A. Rörig ; A. Rouzée ; C. Vallance ; F. Ziaee ; M. Burt  



J. Chem. Phys. 159, 144302 (2023)
<https://doi.org/10.1063/5.0172749>



View
Online



Export
Citation

CrossMark

Articles You May Be Interested In

Solvent dependent branching between C-I and C-Br bond cleavage following 266 nm excitation of CH₂BrI

J. Chem. Phys. (November 2013)

Excited state dynamics of CH₂I₂ and CH₂BrI studied with UV pump VUV probe photoelectron spectroscopy

J. Chem. Phys. (May 2019)

Photofragmentation spectra of halogenated methanes in the VUV photon energy range

J. Chem. Phys. (May 2014)

500 kHz or 8.5 GHz?
And all the ranges in between.

Lock-in Amplifiers for your periodic signal measurements



Find out more

 Zurich
Instruments

Characterizing the multi-dimensional reaction dynamics of dihalomethanes using XUV-induced Coulomb explosion imaging

Cite as: J. Chem. Phys. 159, 144302 (2023); doi: 10.1063/5.0172749

Submitted: 18 August 2023 • Accepted: 27 September 2023 •

Published Online: 12 October 2023





























View Online



Export Citation



CrossMark

T. Walmsley,¹  J. Unwin,¹  F. Allum,¹  S. Bari,²  R. Boll,³  K. Borne,⁴  M. Brouard,¹  P. Bucksbaum,⁵  N. Ekanayake,²  B. Erk,²  R. Forbes,^{5,6}  A. J. Howard,⁵  P. Eng-Johnsson,⁷  J. W. L. Lee,²  Z. Liu,¹  B. Manschwetus,²  R. Mason,¹  C. Passow,²  J. Peschel,⁷  D. Rivas,³  D. Rolles,⁴  A. Rörig,³  A. Rouzée,⁸  C. Vallance,¹  F. Ziaee,⁴  and M. Burt^{1,a)} 

AFFILIATIONS

¹Chemistry Research Laboratory, Department of Chemistry, University of Oxford, Oxford OX1 3TA, United Kingdom

²Deutsches Elektronen-Synchrotron DESY, Notkestr. 85, 22607 Hamburg, Germany

³European XFEL, Holzkoppel 4, 22869 Schenefeld, Germany

⁴J. R. Macdonald Laboratory, Department of Physics, Kansas State University, Manhattan, Kansas 66506, USA

⁵Stanford PULSE Institute, SLAC National Accelerator Laboratory, 2575 Sand Hill Road, Menlo Park, California 94025, USA

⁶Linac Coherent Light Source, SLAC National Accelerator Laboratory, 2575 Sand Hill Road, Menlo Park, California 94025, USA

⁷Department of Physics, Lund University, 22100 Lund, Sweden

⁸Max-Born-Institute, Max-Born-Straße 2A, 12489 Berlin, Germany

^{a)}Author to whom correspondence should be addressed: michael.burt@chem.ox.ac.uk

ABSTRACT

Site-selective probing of iodine 4d orbitals at 13.1 nm was used to characterize the photolysis of CH₂I₂ and CH₂BrI initiated at 202.5 nm. Time-dependent fragment ion momenta were recorded using Coulomb explosion imaging mass spectrometry and used to determine the structural dynamics of the dissociating molecules. Correlations between these fragment momenta, as well as the onset times of electron transfer reactions between them, indicate that each molecule can undergo neutral three-body photolysis. For CH₂I₂, the structural evolution of the neutral molecule was simultaneously characterized along the C–I and I–C–I coordinates, demonstrating the sensitivity of these measurements to nuclear motion along multiple degrees of freedom.

© 2023 Author(s). All article content, except where otherwise noted, is licensed under a Creative Commons Attribution (CC BY) license (<http://creativecommons.org/licenses/by/4.0/>). <https://doi.org/10.1063/5.0172749>

I. INTRODUCTION

X-rays and extreme ultraviolet (XUV) light can site-selectively ionize atomic core electrons. During this process, an inner-shell vacancy is created that can decay through the Auger–Meitner effect to produce a multiply-charged cation.^{1–3} The excitation is initially localized, but the resulting charge rapidly redistributes across the molecule, causing fragmentation via Coulomb explosion. The fragment momenta remain sensitive to the initial nuclear configuration of the molecule, allowing its structure to be determined. For this reason, ultraviolet (UV)-pump/XUV-probe schemes are useful

tools for mapping structural dynamics.^{4–6} The pump pulse initiates the reaction of interest, and one or more of the fragments are then site-selectively probed through inner-shell ionization. At short pump-probe delays, neutral and highly-charged ionic fragments can be close together, which additionally allows electron transfer between fragments to be explored. Recent applications have focused primarily on understanding how these measurements can be used to map known reaction pathways, typically along a single degree of freedom.^{3,7,8} In this report, we exploit inner-shell ionization to distinguish more complex three-body processes, by probing the halomethane photochemistry of CH₂I₂ and CH₂BrI.

Halomethanes are model systems for photochemistry. They undergo some of the simplest unimolecular reactions and contribute to the dynamics of sea spray aerosol formation and ozone depletion.^{9–16} The photochemistry of CH₃X derivatives (where X is a halogen) primarily follows linear and ballistic photolysis mechanisms along the C–X bond axis.^{17–21} By contrast, the reaction dynamics of CH₂X₂ derivatives are more complex, with the second halogen atom allowing for sequential or concerted fragmentation mechanisms at wavelengths below 250 nm, as well as isomerization.^{22–24} As a consequence, these molecules are ideal targets for assessing the ability of inner-shell ionization to simultaneously measure structural changes along multiple degrees of freedom.

Here, the UV-induced dynamics of CH₂I₂ and CH₂BrI are initiated at 202.5 nm (6.1 eV) and probed at 13.1 nm (94 eV) using inner-shell ionization at the I 4d absorption edge. The pump wavelength can access the 2A₁-band of CH₂I₂, which reaches an absorbance maximum at 214 nm, as shown in Fig. 1.^{25,26} This energy is sufficient to overcome the ground and excited spin–orbit state dissociation thresholds (D_0 and D_*) of both C–I bonds (CH₂I₂: $D_{0/*} = 2.155/3.098$ eV; CH₂I: $D_0 = 2.834$ eV),²⁷ which are initially in a ground-state configuration with C_{2v} symmetry. Similarly, the B-band of CH₂BrI reaches a maximum at 218 nm and single-photon absorption at this wavelength also allows both C–X bonds to cleave. Prior work by Lee and co-workers at 210 nm indicates that primary C–Br dissociation ($D_{0/*} = 2.936/3.391$ eV) and three-body fragmentation are expected to occur about 61% and 33% of the time, respectively.²³ Three-body fragmentation mechanisms producing two free halogen atoms (illustrated in Fig. 1) are therefore expected for each molecule, offering multiple sites for XUV-induced ionization and electron transfer.

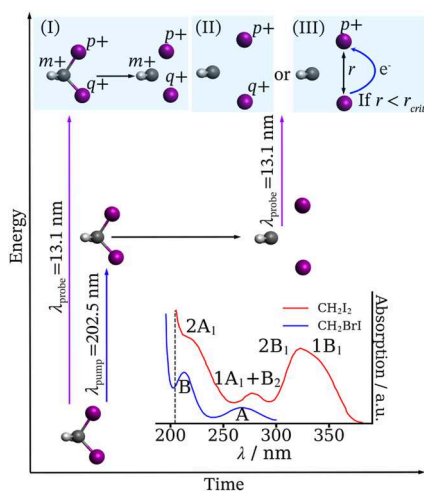


FIG. 1. A schematic depicting the three-body reactions of CH₂I₂ (C = grey, H = white, I = purple) discussed in this study. These include XUV-induced ionization and Coulomb explosion of the ground state (I), where charges (m, p, q) can be found on multiple fragments, as well as ionization following three-body dissociation at 202.5 nm, leading to Coulombic repulsion (II) or electron transfer (III) between fragments. Similar outcomes can occur for CH₂BrI. For CH₂I₂ and CH₂BrI, UV excitation occurs to the 2A₁- and B-bands, respectively, as demonstrated by their inset absorption spectra.^{23,25,26}

By preferentially ionizing halogen substituents at different delays after they dissociate, the probability of electron transfer from a neutral radical to a halogen cation can be investigated as a function of pump-probe delay and hence internuclear distance.^{3,7,8} For CH₃I, which has an approximately ballistic dissociation mechanism, the probability of electron transfer from the methyl radical to a multiply charged iodine cation has been successfully modeled by a classical over-the-barrier (COB) model, where the critical distance (r_{crit}) beyond which the barrier to electron transfer becomes energetically unfavourable depends only on the charge of the electron acceptor and the ionization potential (IP) of the neutral electron donor.^{3,28–30} This is described by the following equation, where n is the charge number, e is the elementary charge and k is the Coulomb constant.

$$r_{\text{crit}} = ke^2 \frac{1 + 2\sqrt{ne}}{\text{IP}} \quad (1)$$

In the following experiments, electron transfer reactions are observed following UV excitation and XUV probe spectroscopy for I^{n+} states produced from CH₂I₂ ($n = 2–5$) and CH₂BrI ($n = 2–4$), as well as Br²⁺. For CH₂I₂, the onset times and fragment kinetic energies of these features are used in conjunction with correlated and time-dependent fragment ion yields to deduce fragment dissociation and separation velocities. The results indicate that CH₂I₂ can undergo a three-body dissociation where both C–I bonds break, with simultaneous structural changes along the I–C–I bending coordinate. Comparisons between CH₂I₂ and CH₂BrI, and with theoretical results obtained from the over-the-barrier electron transfer model, suggest that CH₂BrI exhibits similar behavior.

II. METHODS

Coulomb explosion fragment mass spectra of CH₂I₂ and CH₂BrI were recorded by velocity map imaging (VMI) mass spectrometry using the CAMP end station at FLASH BL1.^{31,32} Molecular beams of each target were individually expanded into the CAMP experimental chamber as continuous jets via two skimmers. The CH₂I₂ beam was additionally seeded with He gas. The molecular beams were intersected perpendicularly by the FLASH XUV pulse ($\lambda_{\text{probe}} = 13.1$ nm, bandwidth = 0.1 nm [full width half maximum (FWHM)]) and by the frequency-quadrupled output of the FLASH pump-probe laser system ($\lambda_{\text{pump}} = 202.5$ nm, bandwidth = 0.75 nm (FWHM)).³³ Both beams were horizontally polarized parallel to the detector plane of the VMI spectrometer. The probe wavelength was chosen to ensure site-selective ionization of I 4d orbitals belonging to the target molecules.^{34,35} The I 4d absorption cross section at 13.1 nm is about 10 Mb, whereas that of the Br 3d orbitals is roughly 1.5 Mb.³⁶ The average XUV pulse energies were 26 ± 6 and 33 ± 6 μJ during the CH₂I₂ and CH₂BrI experiments, which were reduced to 1.8 ± 0.4 and 2.1 ± 0.4 μJ by respectively passing the beams through a pair of niobium and zirconium filters, with thicknesses of 384 and 202 nm, or a 101 nm aluminium filter.³⁷ The XUV pulse energy distributions are given for each molecule in Fig. S1 of the supplementary material. The XUV pulse duration and focused beam size within the VMI chamber were estimated to be 50–60 fs and 10 μm respectively, based on previous measurements,^{31,38} yielding intensities of 8.3×10^{13} and 9.7×10^{13} W cm⁻² for the CH₂I₂ and CH₂BrI experiments.

The pump wavelength was generated from the 810 nm output of the FLASH1 pump-probe laser system, which comprises a Ti:sapphire oscillator (Quantum Gecco) and a 10 Hz chirped pulse amplifier (Coherent Hydra-25). This provided 12 mJ, 57 ± 3 fs infrared (IR) pulses, an 8 mJ fraction of which was passed through a 50/50 beamsplitter. The reflected beam was frequency tripled by a pair of β -BaB₂O₄ (BBO) crystals and separated from the fundamental frequency using a series of dichroic mirrors. The transmitted beam was further split by a second 50/50 beamsplitter; one component was recombined with the third harmonic in a BBO crystal to produce the fourth harmonic through sum-frequency generation, while the other was retained for cross-correlation measurements. The resulting 202.5 nm output was then separated from the fundamental and third harmonic frequencies by passing the beam through a second set of dichroic mirrors. Approximate average pump pulse energies for the CH₂I₂ and CH₂BrI experiments were 6 and 2.5 μ J, respectively. These were attenuated to 2.7 and 1.1 μ J, respectively, according to the transmission of the beamline after measurement (~45%). The corresponding FWHM pulse durations of each experiment were determined to be 143 ± 15 and 157 ± 18 fs from cross-correlations of the overlap between the fourth harmonic and fundamental pulses in xenon gas, which produced a transient Xe⁺ signal due to two-color multiphoton ionization.⁷ The pump pulse focal diameter in the VMI chamber was 38 μ m, resulting in Gaussian pump pulse intensities of 3.3×10^{12} and 1.3×10^{12} W cm⁻² for the CH₂I₂ and CH₂BrI experiments, respectively.

A computer-controlled delay stage placed in the main infrared beamline was used to adjust the relative arrival times of the UV and XUV pulses in the VMI spectrometer. Fluctuations in the XUV pulse arrival times relative to this stage were corrected for using the bunch arrival monitor installed before the FLASH undulator.^{39,40} The CH₂I₂ measurements were acquired in 50 fs steps around the UV/XUV overlap time and in 200 fs steps from 3 ps onward. The CH₂BrI data was acquired in 50 fs steps. In this report, a positive delay time corresponds to the UV pulse preceding the XUV pulse. The overlap time (or zero delay, t_0) was determined using a two-step process involving xenon gas: first, the UV/IR t_0 was determined by a cross-correlation measurement of the Xe⁺ yield as a function of the UV/IR delay; second, the IR/XUV t_0 was identified by monitoring the time-dependent Xe²⁺ and Xe³⁺ yields, produced by the ionization of Xe by the IR and XUV laser pulses, and fitting them to a normal cumulative distribution function (CDF). In this latter measurement, XUV-induced Xe 4d ionization and Auger-Meitner decay produced Xe²⁺, which was then further ionized to Xe³⁺ by the IR pulse.^{41,42} Collectively, these procedures allowed the UV/XUV overlap time to be determined. Time-dependent IR/XUV xenon measurements were recorded both before and periodically throughout the experiments to ensure this time overlap remained consistent.

Ions produced in the VMI interaction region were separated by their times-of-flight and projected onto two chevron-stacked microchannel plates positioned in front of a P47 phosphor screen (Photonis). The positions (x , y) and arrival times (t) of the light emitted by the phosphor screen were detected by a Pixel Imaging Mass Spectrometry (PImMS) camera installed with a 324×324 pixel² PImMS2 sensor with 25 ns timing precision. As incident photons can activate multiple pixels over several time registers, the PImMS2 data was centroided in both space and time to

improve the (x , y , t) assignments.⁴³ The number of counts per XUV laser shot were further normalized by the XUV pulse energies measured by the FLASH gas monitor detector.^{40,44} Finally, VMI radius-to-momentum calibrations were obtained for various fragment ion charge states by modeling the ion trajectories within the spectrometer using SIMION 8.1.⁴⁵

III. RESULTS AND DISCUSSION

Mass spectra collected following the interactions of CH₂I₂ and CH₂BrI with the XUV beam are shown in Fig. 2. For both molecules, XUV ionization produced I^{*n*+} fragments up to at least $n = 5$, with decreasing yields as the charge state increases. For comparison, single-photon ionization experiments on Xe at a similar photon energy demonstrated that only charge states up to Xe³⁺ are accessible.⁴⁶ As Xe is isoelectronic with I⁻, it is likely that single-photon I 4d ionization at 13.1 nm produces similar outcomes following Auger-Meitner decay. Higher I^{*n*+} charge states are therefore attributed to XUV multiphoton absorption. CH₂I⁺ and CH₂⁺ fragments are also observed in the mass spectra for both molecules, as are the respective dihalogen cations (I₂⁺ and BrI⁺). The CH₂BrI mass spectrum additionally exhibits signatures corresponding to CH₂Br⁺, Br⁺, and Br²⁺ (as well as a small amount of CH₂I₂ contamination). As will be discussed below, these observations can largely be attributed to Coulomb explosions of highly-charged parent ions produced by site-selective ionization of the I 4d orbital. Direct ionization of the bromine atoms is a smaller contribution as the relevant ionization cross sections are one order of magnitude lower at 13.1 nm.^{36,46}

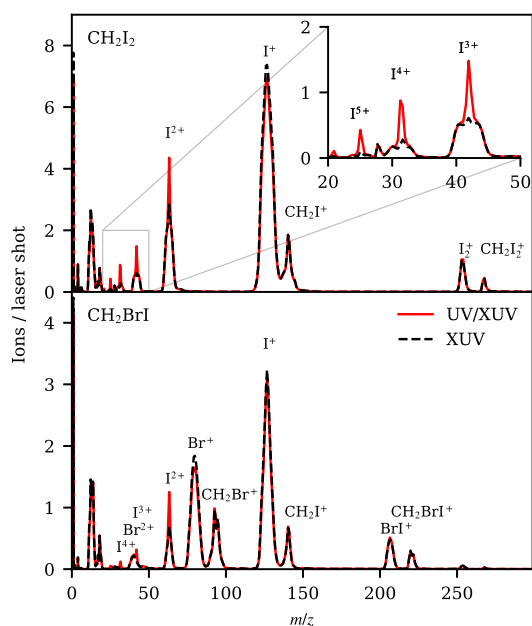


FIG. 2. Mass spectra of CH₂I₂ and CH₂BrI for the XUV probe (black) and UV/XUV pump-probe (red) experiments. The latter are integrated over all positive pump-probe delays.

The UV/XUV mass spectra for CH_2I_2 and CH_2BrI , integrated over all positive delays, are also shown in Fig. 2. Small but clear changes relative to the XUV spectra are observed due to UV excitation, particularly in the I^{n+} ($n = 2-5$) signals. This is similar to the response of CH_3I to excitation and ionization at comparable photon energies.⁷ Singly-charged fragments from CH_2I_2 and CH_2BrI (I^+ , Br^+ , BrI^+ , I_2^+ , CH_2I^+ , and CH_2Br^+) remain unchanged or decrease in intensity relative to the XUV-only spectra.

Figures 3 and 4 display the time-resolved momentum distributions for the CH_2I_2 and CH_2BrI fragments that exhibit two-color signals. These were created by integrating the fragment velocity-map ion images over their angular coordinates, and subtracting contributions from negative (XUV-early) pump-probe delays. It should be cautioned that, as Figs. 3 and 4 are produced from two-dimensional projections of three-dimensional momenta, they slightly underestimate the true fragment momenta. To account for this, the fragment kinetic energies reported here were obtained from the thin central slices of the respective time-of-flight peaks. This effectively selects ions that are travelling parallel to the detection plane, allowing more accurate ion momenta to be obtained without the need to resort to inverse Abel transformation methods.⁴⁷ As shown in Fig. 3(a), clear depletions of intensity after 0 ps are observed at high momenta for all

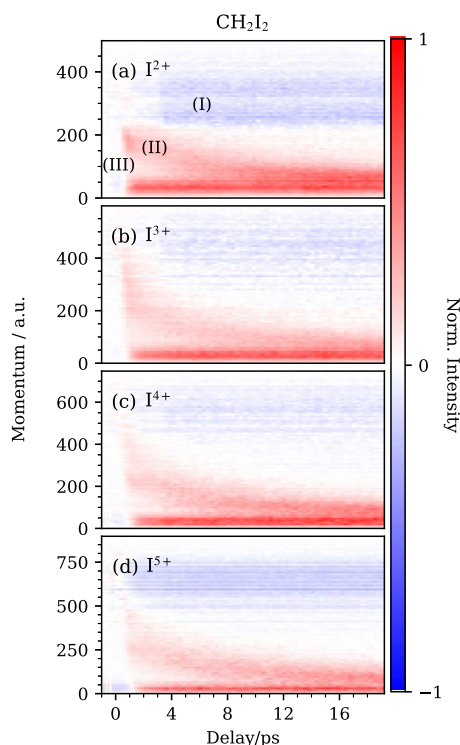


FIG. 3. Time-dependent I^{n+} ($n = 2-5$) momentum distributions produced from CH_2I_2 , recorded in 50 fs and 200 fs steps. Momenta averaged over negative delays were subtracted to highlight changes induced by UV excitation. The intensities of each panel are independently normalized with respect to the number of laser shots and the average XUV pulse energy per delay. An XUV-induced Coulomb explosion (I), a UV-pump/XUV-probe Coulomb explosion (II), and a low momentum dissociative channel (III) are labelled in (a) for clarity, but are also visible in (b)–(d).

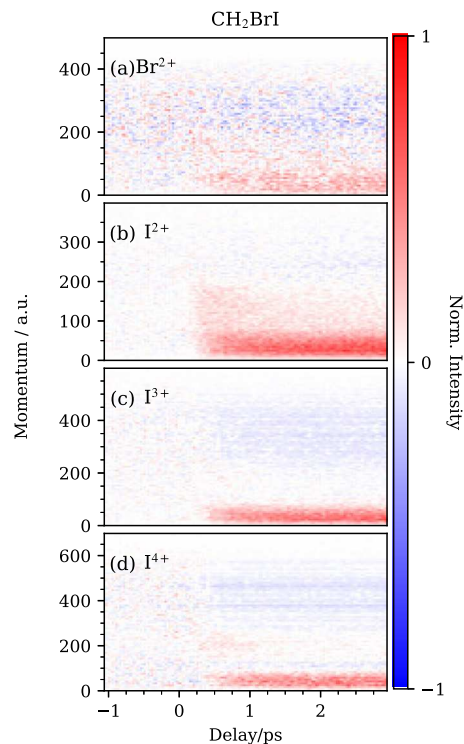


FIG. 4. Time-dependent Br^{2+} and I^{n+} ($n = 2-4$) momentum distributions produced from CH_2BrI , recorded in 50 fs steps. Momenta averaged over negative delays were subtracted. The intensities of each panel are independently normalized with respect to the number of laser shots and to the integrated XUV pulse energy per delay.

ionic fragments, while enhancements are evident at lower momenta. Three time-dependent channels are distinguishable, corresponding to those introduced in Fig. 1. Channel I primarily occurs from XUV-induced Coulomb explosion of the ground-state molecule and hence depletes after a portion of the molecules are excited by the UV pulse at t_0 . However, we note that in the case of I^{2+} from CH_2I_2 , this feature may mask contributions from the concerted elimination of I_2 , which has been observed at 198 nm using a UV/IR scheme.⁴⁸ Channels II and III represent UV-induced neutral photolysis followed by XUV ionization of the free halogen atoms, as has been demonstrated previously.^{20,22} The following sections justify these assignments in greater detail.

A. Time-resolved photofragment ion yields

The UV-induced ion yield enhancements in Fig. 3 fall into two categories: initially high momentum channels that decrease to asymptotes with increasing pump-probe delay (II), and low-momentum signatures (III) that appear within a few hundred femtoseconds after excitation and remain constant.

Channel II appears when an XUV pulse produces at least two charged fragments that repel from one another. For each target molecule, single-photon absorption at 202.5 nm provides sufficient energy to break both carbon-halogen bonds. At short pump-probe

delays, these neutral fragments are spatially close and experience significant mutual Coulombic repulsion following XUV ionization. As their internuclear separation increases over time, ionization leads to weaker repulsion between the ionized fragments at longer delays and hence results in lower fragment momenta.^{22,49} This outcome is only clearly observed for CH₂I₂, as its dissociation produces two iodine-containing fragments that can each be readily ionized by an XUV photon. At a given pump-probe delay, the total kinetic energy T of the fragments produced from these reactions depends on the UV photon energy $h\nu$, the dissociation energies D_0 of any bonds broken, the energy distributed to the excitation of internal modes E_{int}^* , and the electrostatic potential energy arising from pairwise interactions between charges q_i and q_j with separations r_{ij} . This is shown in the following equation, where k is the Coulomb constant:

$$T = h\nu - E_{\text{int}}^* - \sum D_0 + \sum_{j \neq i}^n \frac{kq_i q_j}{r_{ij}}. \quad (2)$$

By contrast, channel III arises when the XUV pulse ionizes only one dissociation product. This is confirmed by the constant momenta of these features, which solely represent the momenta of the neutral halogens produced following UV photolysis. As the fragment separation increases with pump-probe delay, the onset times (t_{crit}) of these channels represent the critical internuclear distances (r_{crit}) at which electron donation between the participating fragments becomes unfavourable. This is consistent with the classical over-the-barrier electron-transfer model for a two-body system involving a neutral and an ion.^{28–30} At distances shorter than the critical separation, the neutral fragment can donate a valence electron to the iodine ion. At longer distances, the potential barrier associated with this process becomes too large and the electron stays bound to the neutral fragment. The delayed onset of a particular X^{n+} channel therefore implies that it exists as $X^{(n-1)+}$ after the halogen is ionized, but before reaching its critical separation point. Similar features have been observed and characterized for several haloalkanes, including CH₃I and CH₂BrI, as well as the aryl trihalide C₆H₃F₂I.^{3,7,8,50}

B. Photodissociation and Coulombic repulsion

The time-dependent Coulomb repulsion shown in Fig. 3 (channel II) is assigned to interactions between pairs of I^{n+} ($n = 2–5$) fragments produced following UV-induced neutral CH₂I₂ photolysis and subsequent XUV ionization of the released iodines. In each case, iodine atoms were ionized by the XUV beam to a distribution of charge states, meaning that the I^{n+} curves are potentially amalgamations of several charge pairs. For CH₂I₂, an iodine ion of a given charge state can be produced with a second iodine ion in any one of its accessible charge states. Because of the broad overlapping energy distributions released by the explosions between each of these charge pairs, individual reaction channels are difficult to assign directly from the data in Fig. 3. However, they can be identified clearly through covariance analysis, which measures how relative variations in two signals correlate. For two fragments, a positive covariance indicates that the ions are, on average, produced through the same mechanism.

In this report, the recoil-frame covariance method is used to place the ions into a common reference frame while retaining

their momentum information.^{43,51–53} Applying this process at each pump-probe delay allows covariant fragment kinetic energy distributions to be created from the resulting recoil-frame images, similar to the process used in Figs. 3 and 4. In this case, kinetic energies were obtained by performing covariance analysis on ions whose arrival times were narrowly distributed around the centres of their respective time-of-flight peaks. As an example, Fig. 5(a) displays the time-dependent kinetic energies obtained as positive covariance when I^{4+} is paired with another I^{4+} . The individual covariance results for the full set of iodine charge states, provided in Fig. S2 of the supplementary material, exhibit similar results. Covariance analysis confirms that, following UV-induced photolysis and XUV ionization, each I^{n+} fragment experiences Coulomb repulsion from a partner iodine ion in any of one of the accessible charge states ($n = 2–5$). The decreasing kinetic energies therefore represent the increasing iodine-iodine separation over time. The time-dependent recoil-frame covariance features of the I^{n+} pairs indicate that the XUV pulse ionizes mainly the iodines, leaving the methylene group neutral. The mutual repulsion between the two iodine ions then results in back-to-back I^{n+} recoil, as is shown in the cov(I^{4+} , I^{4+}) recoil-frame map in Fig. 5(b). The recoil-frame covariance maps for each pair of iodine charge states are provided in Fig. S3, and exhibit the same feature.

To further support the above assignment, it is useful to consider the asymptotic values of the covariant time-dependent kinetic energy distributions obtained for each I^{n+} ($n = 2–5$) pair.

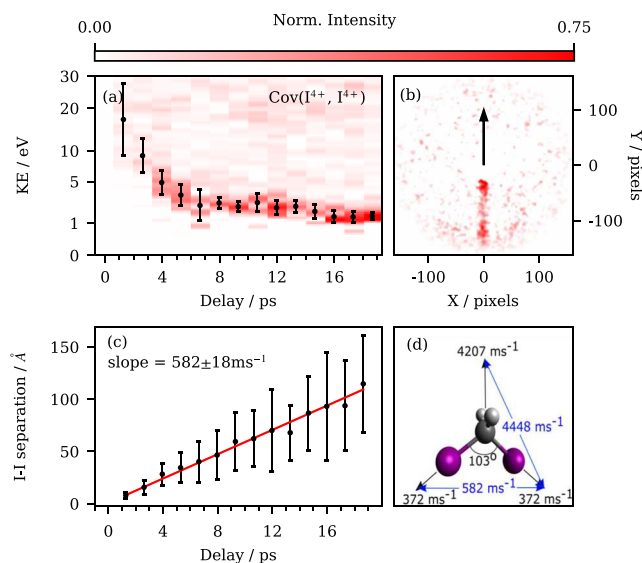


FIG. 5. (a) The time-dependent covariant kinetic energy distribution of two I^{4+} ions, obtained following recoil-frame covariance analysis. (b) The recoil-frame cov(I^{4+} , I^{4+}) image determined over all pump-probe delays, the black arrow indicates the recoil direction of the reference ion. The relative fragment distributions are shown by the positive covariance, negative covariances were set to zero for clarity. (c) The time-dependent covariant kinetic energies obtained for all combinations of $I^{2–5+}$ charge states (Fig. S2) were converted into I–I internuclear distances and averaged, resulting in a linear relationship between I–I separation and delay. (d) A schematic showing the dissociation and separation velocities of the products produced by concerted three-body CH₂I₂ dissociation.

As mentioned in Sec. III A, these asymptotes are the regions over which the Coulombic interactions have become negligible, and therefore represent the translational energies of the neutral iodines gained following dissociation. In these experiments, the kinetic energies observed at long delays were found to increase with the product of the iodine charge states, suggesting that significant contributions from electrostatic repulsion persisted over the 18 ps range that was measured. It was consequently not possible to directly determine the neutral photofragment momenta of the iodines from these asymptotes. To circumvent this, features II and III were instead considered together. As will be detailed below, they arise from the same underlying neutral mechanism, so the momentum of the latter channel is the asymptote of the former. The average kinetic energy obtained by fitting feature III in the I^{n+} data (Fig. 3) was 0.074 ± 0.003 eV. The Gaussian distribution of ion energies had a corresponding standard deviation σ of 0.035 eV. This value agrees closely with that expected for a concerted three-body dissociation, where the methylene group has little internal excitation.⁴⁸ By contrast, it is significantly lower than that predicted for a two-body dissociation at 202.5 nm, where 80%–90% of the available energy should be partitioned into the internal modes of CH_2I .^{25,26,54,55} This would leave only 0.15–0.41 eV for the iodine atom, depending on whether it is created in its ground or spin-orbit excited state. As such, features II and III can both be assigned to the same UV-induced reaction mechanism.

Because only one neutral iodine dissociation velocity was distinguished, the appearance of one time-dependent Coulomb explosion channel per iodine charge pair can be attributed to a concerted dissociation mechanism that produces iodine atoms with approximately equal velocities. As the methylene center of mass is equidistant from the two iodine atoms, its rotational excitation should remain low during a concerted dissociation. By contrast, if the two C–I bonds were to break sequentially, two distinct iodine velocities would be expected for primary and secondary C–I cleavage as the primary CH_2I fragment would receive significant rotational excitation and impart a smaller amount of momentum to an iodine produced through secondary dissociation. This has been detailed previously for other dihalomethanes.^{20,22} The assignment of concerted dissociation is also supported by the behavior of CF_2I_2 , which has similar symmetry to CH_2I_2 and whose three-body dissociation is sequential at 304 nm, but becomes concerted as the wavelength is shortened to 248 nm.^{56,57} Even so, it is worth noting that the broad standard deviation obtained for the neutral iodine velocity may suggest that there is some degree of asynchronicity to the dissociation.

By using the asymptotic neutral iodine velocity extracted experimentally from channel III, the time-dependent kinetic energy distributions of each covariant I^{n+} pair were converted to internuclear distances using Eq. (2). The iodine-iodine separations, averaged over all covariant pairs of iodine charge states [Fig. 5(c)], exhibit the same linear relationship with pump-probe delay. This indicates they all originate from the same neutral mechanism: following UV-induced photolysis, the two neutral iodine atoms promptly accelerate within the precision of the data in Fig. 5 (200 fs), and then propagate at a constant velocity.

The distance between the two recoiling I^{n+} fragments depends on their bond dissociation vectors with the neutral methylene as well as on the force produced by Coulombic repulsion. Since CH_2I_2

has a nonlinear geometry, these two directions do not coincide for a three-body dissociation [Fig. 5(d)]. However, the results in Fig. 5(c) can be used to separate these contributions and characterize the neutral dissociation mechanism. The kinetic energy of channel III (0.074 ± 0.003 eV) corresponds to a neutral photofragment velocity of 372 ± 13 ms^{-1} , which gives a good estimation of the velocity of both iodine atoms produced in a concerted three-body dissociation. A linear regression of the time-dependent internuclear separation shown in Fig. 5(c) indicates that the two iodines separate with a velocity of 582 ± 18 ms^{-1} . Together, these values correspond to an I–C–I angle of $102.9^\circ \pm 6.8^\circ$ for the neutral three-body dissociation [Fig. 5(d)]. This is smaller, but comparable to, the neutral equilibrium geometry (116°),¹⁰ which was confirmed in these experiments by three-body covariance analysis of the XUV-induced Coulomb explosion of ground-state CH_2I_2 (see Sec. III of the supplementary material for further details). We note that multiple excited states can be accessed by the UV pulse,⁵⁸ and therefore we expect that the experimentally determined I–C–I angle represents an average value over the different states that can be populated.⁵⁹ Time-dependent momentum distributions, provided in Fig. S4 of the supplementary material, are calculated for each pair of iodine charge states using the separation velocities and I–C–I recoil angle obtained from covariance analysis in conjunction with channel III. A good agreement is observed between the experimental and predicted ion distributions, which are calculated under the assumption that CH_2I_2 undergoes a concerted three-body dissociation.

C. Electron-transfer reactions

As previously mentioned, low momentum channels delayed relative to the UV/XUV overlap time (feature III) were exhibited by the I^{n+} fragments of CH_2I_2 and CH_2BrI , as well as by Br^{2+} . These indicate that, following the arrival of the UV and XUV pulses, electron transfer occurs between a neutral moiety and a charged fragment. For CH_2I_2 , the I^{n+} kinetic energies were determined to be 0.074 ± 0.003 eV, as described above. Similarly, only one signature was observed for each of the iodine and bromine fragments of CH_2BrI . Their kinetic energies, obtained from the measured $I^{2/3+}$ and Br^{2+} momenta, were 0.086 ± 0.003 eV ($\sigma = 0.047$ eV) for iodine (averaged over the two ions) and 0.18 ± 0.014 eV ($\sigma = 0.12$ eV) for bromine, corresponding to dissociation velocities of 367 ± 13 and 664 ± 54 ms^{-1} , respectively. The onset times of electron transfer for each ion shown in Figs. 3 and 4 were determined by fitting the corresponding observed ion yields using a CDF. An example of this process is shown in Fig. 6 for I^{3+} from CH_2I_2 , which reproduces the low momentum range of Fig. 3(b) with 50 fs precision. The corresponding analysis performed for the other fragments produced from CH_2I_2 and CH_2BrI are provided in Figs. S5 and S6.

The onset times for each channel observed in CH_2I_2 are collected in Table I. These lengthen from 0.76 ± 0.015 to 1.27 ± 0.022 ps as the iodine charge state increases from +2 to +5. This is consistent with the COB model, which predicts longer critical distances at higher charges due to the greater Coulombic attraction. The longest distance where electron transfer is still classically possible is the point where the height of the reaction barrier is equal to the ionization potential of the fragment that donates the electron.²⁹ This value can be determined by assigning the reaction mechanism and converting t_{crit} to r_{crit} .

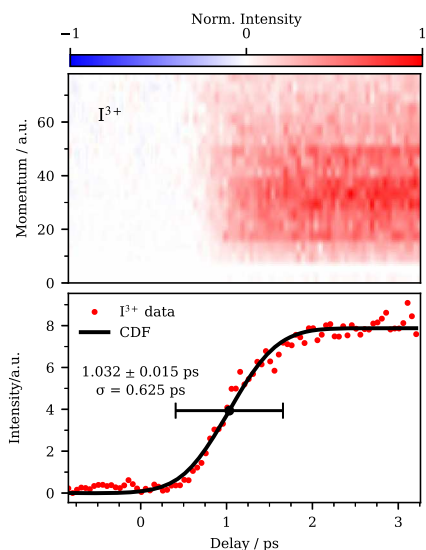


FIG. 6. The low momentum ion yield of I^{3+} produced following the photolysis of CH_2I_2 , given in 50 fs increments. The average momentum distribution at negative pump-probe delays has been subtracted to remove XUV-early contributions. The onset of this channel indicates electron transfer, and was determined from the integrated ion yield using a Gaussian CDF. The Gaussian center, with associated fitting error, as well as the standard deviation of the step function are also shown.

TABLE I. Observed and predicted parameters, using the classical over-the-barrier (COB) model,³ for I^{n+} electron transfer following the photolysis of CH_2I_2 at 202.5 nm and the subsequent site-selective ionization of iodine at 13.1 nm.

I^{n+}	Exp. t_{crit} (ps)	Exp. r_{crit} (Å)	COB t_{crit} (ps)	COB r_{crit} (Å)
I^{2+}	0.76 ± 0.015	4.42 ± 0.22	0.91 ± 0.03	5.28
I^{3+}	1.03 ± 0.015	5.99 ± 0.27	1.06 ± 0.03	6.15
I^{4+}	1.17 ± 0.026	6.81 ± 0.35	1.18 ± 0.04	6.89
I^{5+}	1.27 ± 0.022	7.39 ± 0.36	1.30 ± 0.04	7.54

Three neutral species could, in principle, participate in electron transfer to the I^{n+} fragments: CH_2I following primary C–I photolysis, or CH_2 and I produced in a three-body process. The former can be ruled out due to the observed iodine dissociation velocity, which is inconsistent with the amount of energy that would be partitioned into internal CH_2I modes following two-body dissociation. Electron transfer mechanisms arising from the concerted three-body dissociation of CH_2I_2 can be distinguished using the over-the-barrier model. The ionization potentials of methylene (10.4 eV)^{60,61} and atomic iodine (10.45 eV)^{62,63} return similar critical distances for electron transfer to I^{n+} (e.g. 5.34 and 5.28 Å, respectively, for I^{2+}). However, the I–I and I– CH_2 separation velocities are significantly different: the former was shown to be 582 ± 18 ms⁻¹ in Fig. 5(c), yielding COB t_{crit} values between 0.91 ± 0.03 and 1.30 ± 0.04 ps, depending on the I^{n+} fragment; the latter was determined to be 4448 ± 2431 ms⁻¹ geometrically [see Fig. 5(d)], yielding COB t_{crit} values that range from 0.12 ± 0.06 to 0.17 ± 0.09 ps. As a consequence, we assign the observed channel to concerted three-body dissociation,

followed by XUV ionization of a single iodine and subsequent electron transfer from the remaining neutral iodine. The relatively large standard deviations of the Gaussian step functions shown in Fig. 6 and Fig. S5 correspond to the broad onset times of the charge transfer distributions. This is linked to the wide velocity range obtained for the neutral iodine.

Turning to CH_2BrI , electron transfer is evident in the momentum distributions of Br^{2+} and I^{n+} (Fig. 4). As described above, only a single dissociation velocity was distinguishable for each halogen: 664 ± 54 ms⁻¹ for Br^{2+} and an average of 367 ± 13 ms⁻¹ for I^{n+} . Similar to CH_2I_2 , these observations suggest that neutral bromine and iodine exist after excitation by the UV but before the arrival of the XUV pulse. These velocities are inconsistent with a two-body mechanism. If Br or I were produced through single C–X photolysis of CH_2BrI , then the percentage of available energy partitioned into internal modes of the halomethylene co-fragment would be 90% for C–Br dissociation ($D_{0/*} = 2.936/3.391$ eV), and 95% for C–I dissociation ($D_{0/*} = 2.389/3.33$ eV) based on the observed ion momenta. Previous studies that probed the CH_2BrI A-band found that, following C–I photolysis, 66%–68% of the available energy is partitioned into internal modes,²² and Lee and co-workers showed that the amount of internal excitation occurring during a two body process is consistent across wavelengths.²³ The results shown here predict at least 20% more internal excitation is gained compared to this amount, and this significant difference therefore suggests these features indicate neutral three-body dissociation is occurring, as determined for CH_2I_2 .

Due to the lack of time-dependent Coulomb curves and covariance in the CH_2BrI fragment ion yields, it was not possible to determine the relative neutral fragment separation velocities in a similar manner to CH_2I_2 , as was shown in Fig. 5(d). To further ascertain the reaction mechanism, the neutral halogen dissociation velocities were instead used to calculate the separation velocities expected from two-body dissociation into CH_2X and X , as well as for concerted three-body dissociation into two halogens and CH_2 . These are provided in Table II, along with the corresponding t_{crit} values, which were calculated using the over-the-barrier model. Table II compares these COB t_{crit} values to those obtained from the electron transfer channel in each of the I^{n+} and Br^{2+} momentum distributions, which are also given in Fig. S6. The COB t_{crit} values obtained for both a two-body dissociation and for a three-body dissociation with electron transfer between halogen co-fragments are broadly consistent with the experimentally observed t_{crit} values, although a stronger agreement is seen with the three-body dissociation. The COB model predicts a much smaller t_{crit} for electron transfer from the methylene produced in a three-body dissociation. This is because methylene would be produced with a high velocity, leading to a rapid halogen-methylene fragment separation that reaches the critical distance on a much faster timescale. The comparisons given in Table II, combined with the observation that the measured halogen velocities are lower than would be expected from two-body dissociation, signify that this channel is consistent with UV-induced three-body dissociation of CH_2BrI , followed by XUV ionization and electron transfer between halogen co-fragments. It is worth noting that the timescales for C–I and C–Br dissociation are likely to be different and result in asynchronous bond cleavage. It would be worthwhile to repeat this time-dependent study with an IR probe so that both bromine and iodine fragments can become charged.

TABLE II. Predicted times at which electron transfer is no longer possible according to the classical over-the-barrier (COB) model for various two- and three-body CH₂BrI dissociation channels, determined using expected separation velocities v calculated with the measured Br and I neutral product velocities and compared with the observed t_{crit} values (P = electron donor; Q = electron acceptor).

P/Q ⁿ⁺	v (ms ⁻¹)	COB r_{crit} (Å)	COB t_{crit} (ps)	Exp. t_{crit} (ps)
CH ₂ Br/I ²⁺	860 ± 31	6.40	0.74 ± 0.028	0.45 ± 0.015
CH ₂ Br/I ³⁺	860 ± 31	7.47	0.86 ± 0.031	0.55 ± 0.019
CH ₂ Br/I ⁴⁺	860 ± 31	8.36	0.72 ± 0.035	0.56 ± 0.043
CH ₂ I/Br ²⁺	1040 ± 85	6.56	0.63 ± 0.052	0.39 ± 0.074
Br/I ²⁺	883 ± 333	4.67	0.53 ± 0.20	0.45 ± 0.015
Br/I ³⁺	883 ± 333	5.44	0.62 ± 0.23	0.55 ± 0.019
Br/I ⁴⁺	883 ± 333	6.10	0.69 ± 0.26	0.56 ± 0.043
I/Br ²⁺	883 ± 333	5.28	0.60 ± 0.23	0.39 ± 0.074
CH ₂ /I ²⁺	4210 ± 1200	5.33	0.13 ± 0.037	0.45 ± 0.015
CH ₂ /I ³⁺	4210 ± 1200	6.21	0.15 ± 0.043	0.55 ± 0.019
CH ₂ /I ⁴⁺	4210 ± 1200	6.96	0.17 ± 0.048	0.56 ± 0.043
CH ₂ /Br ²⁺	4420 ± 1200	5.33	0.12 ± 0.033	0.39 ± 0.074

Time-dependent covariance could then be used to confirm the proportion of CH₂BrI that dissociates through two- or three-body mechanisms, as well as the corresponding fragment separation velocities.

IV. CONCLUSION

The UV-induced photolysis of CH₂I₂ and CH₂BrI at 202.5 nm was explored using inner-shell ionization. Time-resolved covariance analysis of Coulomb exploding fragments, as well as onset times arising from electron transfer reactions, were used to assign and characterize three-body dissociation mechanisms. For CH₂I₂, these results were used to extract additional information about the structural evolution of the C–I bonds and I–C–I bending angle. These results point toward the possibility of using time-resolved Coulomb explosion imaging to simultaneously map multiple degrees of freedom during the structural evolution of an initially neutral molecule. In combination with time-resolved photoelectron spectroscopy and particle correlation techniques, this could facilitate the use of high-energy photons to characterize reaction potential energy surfaces.

SUPPLEMENTARY MATERIAL

FLASH pulse energy distributions, covariance calculations, predicted ion momenta, and ion yields for the electron transfer channels are collected in the supplementary material.

ACKNOWLEDGMENTS

We acknowledge DESY (Hamburg, Germany), a member of the Helmholtz Association HGF, for the provision of the experimental facilities. Parts of this research were carried out at FLASH through Proposal No F-20181206 EC. The authors are thankful to the scientific and technical teams at FLASH, especially the FLASH laser group

(FS-LA-Laser Science and Technology) who made these experiments possible. We further acknowledge the Max Planck Society for funding the development and the initial operation of the CAMP end-station within the Max Planck Advanced Study Group at CFEL and for providing this equipment for CAMP@FLASH. The installation of CAMP@FLASH was partially funded by the BMBF Grant Nos. 05K10KT2, 05K13KT2, 05K16KT3, and 05K10KTB from FSP-302. The research was additionally supported by the project CALIPSO-plus under the Grant Agreement No. 730872 from the EU Framework Programme for Research and Innovation HORIZON 2020. M. Burt, Z.L., J.U., and T.W. gratefully acknowledge support from the UK EPSRC (Grant No. EP/S028617/1). T.W. and J.U. additionally thank the EPSRC as well as Jesus College, Oxford and the States of Jersey, respectively, for studentship funding. M. Brouard and C.V. gratefully acknowledge the support of EPSRC Programme Grant No. EP/V026690/1. D.R., K.B., and F.Z. were supported by the Chemical Sciences, Geosciences, and Biosciences Division, Office of Basic Energy Sciences, Office of Science, US Department of Energy under Grant No. DE-FG02-86ER13491. P.E.-J. and J.P. acknowledge support from the Swedish Research Council (Grant No. 2017-04106). S.B. acknowledges funding by the Helmholtz Initiative and Networking Fund. R.F. and F.A. gratefully acknowledge support from the Linac Coherent Light Source, SLAC National Accelerator Laboratory, which is supported by the US Department of Energy, Office of Science, Office of Basic Energy Sciences, under Contract No. DE-AC02-76SF00515. A.J.H. was supported under a Stanford Graduate Fellowship as the 2019 Albion Walter Hewlett Fellow. A CC-BY licence is applied to the author accepted manuscript arising from this submission, in accordance with UKRI open access conditions.

AUTHOR DECLARATIONS

Conflict of Interest

The authors have no conflicts to disclose.

Author Contributions

Experiments were conducted by F.A., S.B., R.B., K.B., N.E., B.E., R.F., A.H., J.L., B.M., R.M., C.P., J.P., D. Rivas, D. Rolles, A. Rörig, A. Rouzée, F. Ziaee, and M. Burt, and were conceptualized and directed by M. Burt. The data was analysed by T.W. and J.U., and the manuscript was written by T.W., J.U., and M. Burt in collaboration with all authors.

T. Walmsley: Formal analysis (equal); Writing – original draft (lead); Writing – review & editing (lead). **J. Unwin:** Formal analysis (equal); Writing – original draft (supporting); Writing – review & editing (supporting). **F. Allum:** Investigation (supporting); Writing – review & editing (supporting). **S. Bari:** Investigation (supporting); Writing – review & editing (supporting). **R. Boll:** Investigation (supporting); Writing – review & editing (supporting). **K. Borne:** Investigation (supporting); Writing – review & editing (supporting). **M. Brouard:** Resources (supporting); Writing – review & editing (supporting). **P. Bucksbaum:** Resources (supporting); Writing – review & editing (supporting). **N. Ekanayake:** Investigation (supporting); Methodology (supporting); Resources (supporting); Writing – review & editing (supporting). **B. Erk:** Investigation (supporting); Methodology (supporting); Project administration (supporting); Resources (supporting); Writing – review & editing (supporting). **R. Forbes:** Investigation (supporting); Methodology (supporting); Writing – review & editing (supporting). **A. J. Howard:** Investigation (supporting); Writing – review & editing (supporting). **P. Eng-Johnsson:** Investigation (supporting); Resources (supporting); Writing – review & editing (supporting). **J. W. L. Lee:** Investigation (supporting); Methodology (supporting); Writing – review & editing (supporting). **Z. Liu:** Formal analysis (supporting); Writing – review & editing (supporting). **B. Manschwetus:** Investigation (supporting); Methodology (supporting); Writing – review & editing (supporting). **R. Mason:** Investigation (supporting); Writing – review & editing (supporting). **C. Passow:** Data curation (supporting); Investigation (supporting); Project administration (supporting); Software (supporting); Writing – review & editing (supporting). **J. Peschel:** Investigation (supporting); Writing – review & editing (supporting). **D. Rivas:** Investigation (supporting); Methodology (supporting); Writing – review & editing (supporting). **D. Rolles:** Investigation (supporting); Writing – review & editing (supporting). **A. Rörig:** Investigation (supporting); Writing – review & editing (supporting). **A. Rouzée:** Investigation (supporting); Methodology (supporting); Writing – review & editing (supporting). **C. Vallance:** Investigation (supporting); Writing – review & editing (supporting). **F. Ziaee:** Investigation (supporting); Writing – review & editing (supporting). **M. Burt:** Conceptualization (lead); Formal analysis (supporting); Funding acquisition (lead); Project administration (lead); Supervision (lead); Writing – original draft (supporting); Writing – review & editing (supporting).

DATA AVAILABILITY

Raw data were generated at the FLASH free electron laser facility. Derived data supporting the findings of this study are available from the corresponding author upon request.

REFERENCES

- ¹K. Siegbahn, *Rev. Mod. Phys.* **54**, 709 (1982).
- ²H. Fukuzawa and K. Ueda, *Adv. Phys.* **X 5**, 1785327 (2020).
- ³B. Erk, R. Boll, S. Trippel, D. Anielski, L. Foucar, B. Rudek, S. W. Epp, R. Coffee, S. Carron, and S. Schorb, *Science* **345**, 288–291 (2014).
- ⁴F. Brauße, G. Goldsztejn, K. Amini, R. Boll, S. Bari, C. Bomme, M. Brouard, M. Burt, B. C. De Miranda, and S. Düsterer, *Phys. Rev. A* **97**, 043429 (2018).
- ⁵H. Köckert, J. W. L. Lee, F. Allum, K. Amini, S. Bari, C. Bomme, F. Brauße, M. Brouard, M. Burt, and B. C. De Miranda, *J. Phys. B: At., Mol. Opt. Phys.* **55**, 014001 (2022).
- ⁶D. Rolles, *Adv. Phys.* **X 8**, 2132182 (2023).
- ⁷R. Forbes, F. Allum, S. Bari, R. Boll, K. Borne, M. Brouard, P. H. Bucksbaum, N. Ekanayake, B. Erk, and A. J. Howard, *J. Phys. B: At., Mol. Opt. Phys.* **53**, 224001 (2020).
- ⁸F. Allum, N. Anders, M. Brouard, P. Bucksbaum, M. Burt, B. Downes-Ward, S. Grundmann, J. Harries, Y. Ishimura, and H. Iwayama, *Faraday Discuss.* **228**, 571–596 (2021).
- ⁹K.-C. Lin and P.-Y. Tsai, *Phys. Chem. Chem. Phys.* **16**, 7184–7198 (2014).
- ¹⁰A. Mandal, P. J. Singh, A. Shastri, and B. N. Jagatap, *J. Chem. Phys.* **140**, 194312 (2014).
- ¹¹S. A. Reid, *Int. Rev. Phys. Chem.* **33**, 341–370 (2014).
- ¹²P. K. Quinn, D. B. Collins, V. H. Grassian, K. A. Prather, and T. S. Bates, *Chem. Rev.* **115**, 4383–4399 (2015).
- ¹³V. A. Borin, S. M. Matveev, D. S. Budkina, P. Z. El-Khoury, and A. N. Tarnovsky, *Phys. Chem. Chem. Phys.* **18**, 28883–28892 (2016).
- ¹⁴R. A. Ingle, C. S. Hansen, E. Elsdon, M. Bain, S. J. King, J. W. L. Lee, M. Brouard, C. Vallance, R. Turchetta, and M. N. R. Ashfold, *J. Chem. Phys.* **147**, 013914 (2017).
- ¹⁵S. Godara and M. Paranjothy, *J. Phys. Chem. A* **123**, 8527–8535 (2019).
- ¹⁶A. R. Casavola, A. Cartoni, M. C. Castrovilli, S. Borocci, P. Bolognesi, J. Chiarinelli, D. Catone, and L. Avaldi, *J. Phys. Chem. A* **124**, 7491–7499 (2020).
- ¹⁷Y. Wang, S. Zhang, Z. Wei, and B. Zhang, *J. Phys. Chem. A* **112**, 3846–3851 (2008).
- ¹⁸M. E. Corrales, G. Gitzinger, J. González-Vázquez, V. Lorient, R. de Nalda, and L. Bañares, *J. Phys. Chem. A* **116**, 2669–2677 (2012).
- ¹⁹K. Motomura, E. Kukuk, H. Fukuzawa, S.-I. Wada, K. Nagaya, S. Ohmura, S. Mondal, T. Tachibana, Y. Ito, and R. Koga, *J. Phys. Chem. Lett.* **6**, 2944–2949 (2015).
- ²⁰F. Allum, M. Burt, K. Amini, R. Boll, H. Köckert, P. K. Olshin, S. Bari, C. Bomme, F. Brauße, B. Cunha de Miranda *et al.*, *J. Chem. Phys.* **149**, 204313 (2018).
- ²¹M. E. Corrales, J. González-Vázquez, R. de Nalda, and L. Bañares, *J. Phys. Chem. Lett.* **10**, 138–143 (2018).
- ²²M. Burt, R. Boll, J. W. L. Lee, K. Amini, H. Köckert, C. Vallance, A. S. Gentleman, S. R. Mackenzie, S. Bari, and C. Bomme, *Phys. Rev. A* **96**, 043415 (2017).
- ²³L. J. Butler, E. J. Hintsa, S. F. Shane, and Y. T. Lee, *J. Chem. Phys.* **86**, 2051–2074 (1987).
- ²⁴S. Lee and R. Bersohn, *J. Phys. Chem.* **86**, 728–730 (1982).
- ²⁵H. Xu, Y. Guo, S. Liu, X. Ma, D. Dai, and G. Sha, *J. Chem. Phys.* **117**, 5722–5729 (2002).
- ²⁶S. L. Baughcum and S. R. Leone, *J. Chem. Phys.* **72**, 6531–6545 (1980).
- ²⁷B. W. Toulson, J. P. Alaniz, J. G. Hill, and C. Murray, *Phys. Chem. Chem. Phys.* **18**, 11091–11103 (2016).
- ²⁸A. Niehaus, *J. Phys. B: At. Mol. Phys.* **19**, 2925 (1986).
- ²⁹R. Boll, B. Erk, R. Coffee, S. Trippel, T. Kierspel, C. Bomme, J. D. Bozek, M. Burkett, S. Carron, K. R. Ferguson *et al.*, *Struct. Dyn.* **3**, 043207 (2016).
- ³⁰H. Ryufuku, K. Sasaki, and T. Watanabe, *Phys. Rev. A* **21**, 745 (1980).
- ³¹B. Erk, J. P. Müller, C. Bomme, R. Boll, G. Brenner, H. N. Chapman, J. Correa, S. Düsterer, S. Dziarzhytski, and S. Eisebitt, *J. Synchrotron Radiat.* **25**, 1529–1540 (2018).
- ³²W. Ackermann, G. Asova, V. Ayvazyan, A. Azima, N. Baboi, J. Bähr, V. Balandin, B. Beutner, A. Brandt, and A. Bolzmann, *Nat. Photonics* **1**, 336–342 (2007).

- ³³H. Redlin, A. Al-Shemmary, A. Azima, N. Stojanovic, F. Tavella, I. Will, and S. Düsterer, *Nucl. Instrum. Methods Phys. Res., Sect. A* **635**, S88–S93 (2011).
- ³⁴T. N. Olney, G. Cooper, and C. E. Brion, *Chem. Phys.* **232**, 211–237 (1998).
- ³⁵R. Forbes, A. De Fanis, D. Rolles, S. T. Pratt, I. Powis, N. A. Besley, A. R. Milosavljević, C. Nicolas, J. D. Bozek, and D. M. P. Holland, *J. Phys. B: At., Mol. Opt. Phys.* **53**, 155101 (2020).
- ³⁶J. Yeh and I. Lindau, *At. Data Nucl. Data Tables* **32**, 1–155 (1985).
- ³⁷F. Canova and L. Poletto, *Optical Technologies for Extreme-Ultraviolet and Soft X-Ray Coherent Sources* (Springer, 2015).
- ³⁸S. Düsterer, M. Rehders, A. Al-Shemmary, C. Behrens, G. Brenner, O. Brovko, M. Dell'Angela, M. Drescher, B. Faatz, J. Feldhaus, U. Frühling, N. Gerasimova, N. Gerken, C. Gerth, T. Golz, A. Grebentsov, E. Hass, K. Honkavaara, V. Kocharian, M. Kurka, T. Limberg, R. Mitzner, R. Moshhammer, E. Plönjes, M. Richter, J. Rönsch-Schulenburg, A. Rudenko, H. Schlarb, B. Schmidt, A. Senfleben, E. A. Schneidmiller, B. Siemer, F. Sorgenfrei, A. A. Sorokin, N. Stojanovic, K. Tiedtke, R. Treusch, M. Vogt, M. Wieland, W. Wurth, S. Wesch, M. Yan, M. V. Yurkov, H. Zacharias, and S. Schreiber, *Phys. Rev. Spec. Top.–Accel. Beams* **17**, 120702 (2014).
- ³⁹A. Angelovski, M. Kuntzsch, M. K. Czwalinna, A. Penirschke, M. Hansli, C. Sydlo, V. Arsov, S. Hunziker, H. Schlarb, and M. Gensch, *Phys. Rev. Spec. Top.–Accel. Beams* **18**, 012801 (2015).
- ⁴⁰E. Savelyev, R. Boll, C. Bomme, N. Schirmel, H. Redlin, B. Erk, S. Düsterer, E. Müller, H. Höppner, and S. Toleikis, *New J. Phys.* **19**, 043009 (2017).
- ⁴¹M. Krikunova, T. Maltezopoulos, A. Azima, M. Schlie, U. Frühling, H. Redlin, R. Kalms, S. Cunovic, N. M. Kabachnik, M. Wieland, and M. Drescher, *New J. Phys.* **11**, 123019 (2009).
- ⁴²D. Rolles, R. Boll, B. Erk, D. Rompotis, and B. Manschwetus, *J. Vis. Exp.* **140**, e57055 (2018).
- ⁴³C. S. Slater, S. Blake, M. Brouard, A. Lauer, C. Vallance, J. J. John, R. Turchetta, A. Nomerotski, L. Christensen, J. H. Nielsen, M. P. Johansson, and H. Stapelfeldt, *Phys. Rev. A* **89**, 011401 (2014).
- ⁴⁴K. Tiedtke, J. Feldhaus, U. Hahn, U. Jastrow, T. Nunez, T. Tschentscher, S. Bobashev, A. Sorokin, J. Hastings, S. Möller *et al.*, *J. Appl. Phys.* **103**, 094511 (2008).
- ⁴⁵D. J. Manura and D. A. Dahl, *SIMION Version 8.0/8.1 User Manual* (Scientific Instrument Services, Inc., 2011).
- ⁴⁶N. Saito and I. H. Suzuki, *Int. J. Mass Spectrom. Ion Processes* **115**, 157–172 (1992).
- ⁴⁷J. J. Lin, J. Zhou, W. Shiu, and K. Liu, *Rev. Sci. Instrum.* **74**, 2495–2500 (2003).
- ⁴⁸F. Ziaee, Ph.D. thesis, Kansas State University, 2022.
- ⁴⁹H. Stapelfeldt, E. Constant, and P. Corkum, *Phys. Rev. Lett.* **74**, 3780 (1995).
- ⁵⁰K. Amini, E. Savelyev, F. Brauße, N. Berrah, C. Bomme, M. Brouard, M. Burt, L. Christensen, S. Düsterer, B. Erk *et al.*, *Struct. Dyn.* **5**, 014301 (2018).
- ⁵¹C. S. Slater, S. Blake, M. Brouard, A. Lauer, C. Vallance, C. S. Bohun, L. Christensen, J. H. Nielsen, M. P. Johansson, and H. Stapelfeldt, *Phys. Rev. A* **91**, 053424 (2015).
- ⁵²C. Vallance, D. Heathcote, and J. W. L. Lee, *J. Phys. Chem. A* **125**, 1117–1133 (2021).
- ⁵³L. Minion, J. W. L. Lee, and M. Burt, *Phys. Chem. Chem. Phys.* **24**, 11636–11645 (2022).
- ⁵⁴C. Fotakis, M. Martin, and R. J. Donovan, *J. Chem. Soc., Faraday Trans. 2* **78**, 1363–1371 (1982).
- ⁵⁵P. M. Kroger, P. C. Demou, and S. J. Riley, *J. Chem. Phys.* **65**, 1823–1834 (1976).
- ⁵⁶K. Bergmann, R. T. Carter, G. E. Hall, and J. R. Huber, *J. Chem. Phys.* **109**, 474–483 (1998).
- ⁵⁷E. A. J. Wannemacher, P. Felder, and J. R. Huber, *J. Chem. Phys.* **95**, 986–997 (1991).
- ⁵⁸S. L. Horton, Y. Liu, R. Forbes, V. Makhija, R. Lausten, A. Stolow, P. Hockett, P. Marquetand, T. Rozgonyi, and T. Weinacht, *J. Chem. Phys.* **150**, 174201 (2019).
- ⁵⁹Y. Liu, T. Rozgonyi, P. Marquetand, and T. Weinacht, *J. Chem. Phys.* **153**, 184304 (2020).
- ⁶⁰G. Herzberg, *Can. J. Phys.* **39**, 1511–1513 (1961).
- ⁶¹W. Reineke and K. Strein, *Rep. Bunsen Soc. Phys. Chem.* **80**, 343–349 (1976).
- ⁶²D. R. Lide, *Handbook of Chemistry and Physics* (CRC Press, 1992), pp. 10–211.
- ⁶³L. Minnhagen, *Ark. Fys.* **21**, 415 (1962).